npj | 2D materials and applications

www.nature.com/npj2dmaterials

ARTICLE OPEN

Investigating heterogeneous defects in single-crystalline WS_2 via tip-enhanced Raman spectroscopy

Chanwoo Lee[1,7], Byeong Geun Jeong[1,2,7], Sung Hyuk Kim[1,2,7], Dong Hyeon Kim[1,2], Seok Joon Yun[1,3], Wooseon Choi[1], Sung-Jin An[1], Dongki Lee[4], Young-Min Kim[1,3], Ki Kang Kim[1,3], Seung Mi Lee[5]✉ and Mun Seok Jeong[2,6]✉

Nanoscale defects in two-dimensional (2D) transition metal dichalcogenides (TMDs) alter their intrinsic optical and electronic properties, and such defects require investigation. Atomic-resolution techniques such as transmission electron microscopy detect nanoscale defects accurately but are limited in terms of clarifying precise chemical and optical characteristics. In this study, we investigated nanoscale heterogeneous defects in a single-crystalline hexagonal WS_2 monolayer using tip-enhanced Raman spectroscopy (TERS). We observed the Raman properties of heterogeneous defects, which are indicated by the shifted $A_1'(\Gamma)$ modes appearing on the W- and S-edge domains, respectively, with defect-induced Raman (D) mode. In the edge region, various Raman features occur with nanoscale defects. In addition, the TERS signals from single-crystalline WS_2 indicate the existence of two majority defects in each domain, which imply S- and W-dominated vacancies. Quantum mechanical computations were performed for each majority defect and demonstrated the defect-induced variation in the vibrational phonon modes. TERS imaging promises to be a powerful technique for determining assorted nanoscale heterogeneous defects as well as for investigating the properties of other nanomaterials.

npj 2D Materials and Applications (2022)6:67 ; https://doi.org/10.1038/s41699-022-00334-4

INTRODUCTION

Layered two-dimensional (2D) semiconductors—most notably, monolayer transition metal dichalcogenides (TMDs)—have attracted significant interest because of their excellent optical and electrical properties[1–5]. Several monolayer TMDs exhibit a direct band gap in the visible wavelength range, which can be attributed to the quantum confinement of carriers at the *K* valleys in the hexagonal Brillouin zone, generating neutral and charged excitons with strong Coulomb interactions[6,7]. These characteristics of TMD materials provide a platform for various applications, such as electronics[1,8,9], valleytronics[7,10–12], and optoelectronics[1,13,14]. Accordingly, mechanically exfoliated TMDs have been widely used as a proof-of-concept for such applications because TMD materials produced by mechanical exfoliation are relatively pristine and have few defects[1,8,15]. Although mechanical exfoliation produces high-quality monolayer TMDs, it is difficult to precisely control their size and number of layers. To overcome these difficulties, a significant amount of research has been conducted on the synthesis of wafer-scale layered 2D materials via chemical vapor deposition (CVD)[16,17]. However, defects in CVD-grown TMDs are inevitable. TMD materials are susceptible to defects such as vacancies[18–23], grain boundaries[24–26], and cracks[27]. These defects can degrade the performance of the TMD material. Thus, it is essential to investigate and understand nanoscale defects in TMD materials because these play a decisive role in the control of the properties of these materials. These nanoscale defects have been studied in hexagonal WS_2 monolayers using scanning transmission electron microscopy (STEM) and conventional Raman and photoluminescence (PL) imaging[18,19]. Jeong et al. and Lin et al. reported that S vacancy (V_S) and W vacancy (V_W) defects mainly exist in the α- and β-domains, respectively, of monolayer WS_2[18,19]. The α- and β-domains represent the W- and S-edge domains, respectively. Although STEM enables the observation of nanoscale defects with atomic resolution, it is technically difficult for conventional imaging to accurately determine the optical properties of nanoscale defects owing to the diffraction limit in the optical system[20,28]. Hence, nanoscale optical imaging techniques such as tip-enhanced Raman spectroscopy (TERS) and tip-enhanced PL are necessary to investigate the intrinsic optical properties of nanoscale defects in TMD materials[20,29–36]. TERS provides Raman scattering information by visualizing the vibrations of individual molecules with a significantly improved spatial resolution compared with confocal Raman spectroscopy[37,38].

In this study, we investigated the Raman properties of heterogeneous defects using scanning tunneling microscopy (STM)-based TERS. We analyzed the single-crystalline WS_2 in each domain with a spatial resolution of ~23 nm. We also measured the energy shift of the vibrational modes in the out-of-plane direction as $A_1'(\Gamma)$ (A_{1g}) in conjunction with the defect-related Raman (D) mode[20], which has also been reported as the $A_1'(M)$ mode[39,40]. Moreover, we spatially differentiated edge defects at the nanoscale level and observed edge-related properties with a correlation between the D and A_{1g} modes within the edge region of monolayer WS_2. Density functional theory (DFT) computations revealed that the heterogeneous majority defects in each domain of the single-crystalline WS_2 exhibit distinctly different Raman characteristics. Moreover, nanoscale TERS imaging determined the optical properties of the lattice vibrations. It indicated that the single-crystalline WS_2 monolayer has S-dominated vacancies ($V_{S\text{-}d}$) and W-dominated vacancies ($V_{W\text{-}d}$) as the heterogeneous majority

[1]Department of Energy Science, Sungkyunkwan University (SKKU), Suwon 16419, Republic of Korea. [2]Department of Physics, Hanyang University (HYU), Seoul 04763, Republic of Korea. [3]Center for Integrated Nanostructure Physics (CINAP), Institute for Basic Science (IBS), Suwon 16419, Republic of Korea. [4]Department of Nanotechnology and Advanced Materials Engineering, Sejong University, Seoul 05006, Korea. [5]Korea Research Institute of Standards and Science (KRISS), Daejeon 34113, Republic of Korea. [6]Department of Energy Engineering, Hanyang University (HYU), Seoul 04763, Republic of Korea. [7]These authors contributed equally: Chanwoo Lee, Byeong Geun Jeong, Sung Hyuk Kim.
✉email: seungmi.lee@kriss.re.kr; mjeong@hanyang.ac.kr

defects in each domain. Furthermore, numerous structural disorders with vacancy (V) defects are present in the edge region.

RESULTS

Raman scattering for single-crystalline WS_2

We synthesized a single-crystalline WS_2 monolayer on a SiO_2/Si substrate using CVD to analyze nanoscale defects according to the domain and edge of WS_2[18]. Monolayer WS_2 was transferred onto an Au substrate using poly (methyl methacrylate) (PMMA) transfer films to perform the STM-TERS experiment. As shown in Fig. 1, the use of Au in a conductive substrate for STM measurement is crucial for TERS measurement owing to the gap-mode effect, which strongly enhances Raman scattering signals (Supplementary Fig. 1)[37,38]. The CVD-grown monolayer WS_2 has two domains (Fig. 1a): α- and β-domains[18,19]. Defects in each WS_2 domain have been reported, which indicates that the α- and β-domains contain V_S and V_W, respectively[18,19]. These defects create different energy levels in the gap states, which affect the PL emission of the WS_2 monolayer[18]. Prior to the TERS measurement, nanoscale defects in the single-crystalline WS_2 monolayer were observed in each domain using atomic-resolution annular dark-field STEM (Supplementary Fig. 2). V_S and V_W were distributed differently in each domain of the single-crystalline WS_2 monolayer.

Using this sample configuration without the TERS tip, as shown in Fig. 1b, we performed confocal Raman imaging of the WS_2 monolayer to observe the α- and β-domains and the edges as well as examine the Raman modes depending on the sites. The confocal Raman images in Fig. 1c and d indicate the area intensity and distribution maps, respectively, for the A_{1g} peak. Figure 1c shows the differences in Raman intensity between the α- and β-domains as well as the strong intensity at the edge of the α-domain. Although there are large differences in intensity between the domains, the shift differential of the Raman frequency value, shown in Fig. 1d, is not prominent. Therefore, we extracted the Raman spectra from Fig. 1c and d to compare the intensities and positions of the Raman peaks, as shown in Fig. 1e–h. The large differences in intensity in the Raman map are a result of the PL emission as the background signal of the Raman spectrum from monolayer WS_2 owing to the resonant excitation of the optical band gap (Supplementary Figs. 3 and 4)[20]. As shown in Fig. 1e–h, the Raman spectra from the middle of the α-domain in Fig. 1e exhibit the strongest Raman intensities among the extracted spectra. Although the α-domain can be regarded as a relatively pristine region owing to the presence of strong Raman signals and non-shifted peaks, the D peak is observed in spectrum 1 in Fig. 1e (see the details in Supplementary Fig. 5). In contrast to the Raman image in Fig. 1c, there is minimal difference in intensity between the α- and β-domains, as shown in Fig. 1e and f, which indicates that PL background signals differ depending on the domain and edge. The extraordinarily strong PL intensity from the monolayer WS_2 edge regions can be attributed to the accumulated and localized excitons[41–43]. The middle regions of the α- and β-domains show relatively high Raman intensities; whereas, the edge regions of the α- and β-domains display weak Raman intensities and low signal-to-noise ratios, as shown in Fig. 1g and h. These phenomena at the edge, where intense PL and weak Raman intensities appear, can be explained by the defective edge regions[41–44]. Notwithstanding the defective sites, the D mode is insignificant owing to the relatively weak Raman intensity. In addition, nanoscale defects cannot be resolved due to the low spatial resolution of confocal Raman imaging.

TERS for heterogeneous defects

We performed TERS mapping of the sample to investigate nanoscale defects in the domain and edge shown in Fig. 1. As shown in Fig. 2a and b, we observed a drastic difference in intensity between the α- and β-domains (which was caused by the PL intensity (see Fig. 1c)) and identified the defective edge regions. The Raman signals with and without Au tip were measured at the same location of the α-domain to demonstrate TERS and the enhancement factor was $\sim 5.4 \times 10^4$ (Supplementary Fig. 6). A normalized TERS intensity profile in Fig. 2c along the yellow solid bar in Fig. 2a was extracted to estimate the spatial resolution of TERS imaging. The intensity profile resolved the boundary edge of the monolayer WS_2 and Au substrate, showing an obvious intensity differential. The derivative of the intensity profile was calculated to precisely measure the spatial resolution using the full width at half-maximum (FWHM) of the fitted Gaussian curve[24]. In accordance with the FWHM, the spatial resolution of the TERS image was estimated to be ~22.7 nm, which is beyond the diffraction limit of the optical system. The spatial resolution of the Raman image was estimated to be ~551 nm using the numerical aperture (NA) of the objective lens (=0.7) and wavelength of the excitation laser (=633 nm)[20]. Thus, the spatial resolution of the TERS image is ~24 times higher than that of the confocal Raman image. In other words, the high-resolution TERS imaging would enable the extraction of information on Raman scattering from numerous defects in a narrow region of tens of nanometers. In addition, the magnified TERS image in Fig. 2b shows the defective edge of the single-crystalline WS_2 monolayer. The confocal Raman images in Fig. 1 do not show a defective edge in the β-domain owing to the limited resolution. These edge defects have a decisive effect on the Raman scattering features, resulting in a low signal-to-noise ratio and the presence of the D mode, as shown in Fig. 1g and h. In the case of mechanically exfoliated multilayer MoS_2 flakes, the edge-induced Raman mode and change in the A_{1g} mode depending on the edge structure type (e.g., zigzag and armchair) are observed[45]. However, the edge-induced Raman peak in the single-crystalline WS_2 monolayer is not significant because the CVD-grown WS_2 flakes are of relatively low quality with inhomogeneous edges. These edge structures possess neither the zigzag nor armchair edges of the homogeneous structure but exhibit structural disorders including a number of defects, such as vacancies, cracks, and broken edges. Thus, we investigated the heterogeneous defects in the domains and edges of the single-crystalline WS_2 monolayer.

On the basis of the TERS images shown in Fig. 2, we extracted other TERS images to investigate the Raman properties of the heterogeneous defects in each domain and edge region of the single-crystalline WS_2 monolayer. We measured the AFM topography and confocal Raman spectroscopy at a wavelength of 532 nm to determine the factors that affect the Raman characteristics and verified that there was no strain effect on the sample by the substrate, indicating that the variations in Raman scattering were caused by defects. (Supplementary Figs. 7–9). Figure 3a shows the peak distribution image of the A_{1g} mode. In contrast to the distribution image of confocal Raman scattering in Fig. 1d, the differences in A_{1g} peak shift between the α- and β-domains are distinct, as shown in Fig. 3a. Although the peak value of the A_{1g} mode for pristine monolayer WS_2 is generally generated at ~417 cm^{-1} [20], the peak distribution of the A_{1g} mode in the α-domain displays a slightly red-shifted A_{1g} peak. This red-shift indicates that the chalcogen atom vacancies in the α-domain (V_S in WS_2), which are the most common defects in TMD materials[18–20], produce an n-doping effect, thus inducing the red-shifted A_{1g} peak[20,46]. Conversely, the Raman signal of the β-domain shows a blue-shifted A_{1g} peak. The blue shift for the A_{1g} mode in TMD materials has been attributed to a p-doped phenomenon that can be generated by metal atom vacancies, namely, V_W in WS_2[46]. In addition, recent research using STEM has demonstrated that $V_{W\text{-}d}$ defects including V_S exist in the β-domain of monolayer WS_2[18,19]. We obtained a skewness image of the A_{1g} peak (Fig. 3b), to investigate the heterogeneous defects in these domains. The D peak, induced in the Raman spectrum of

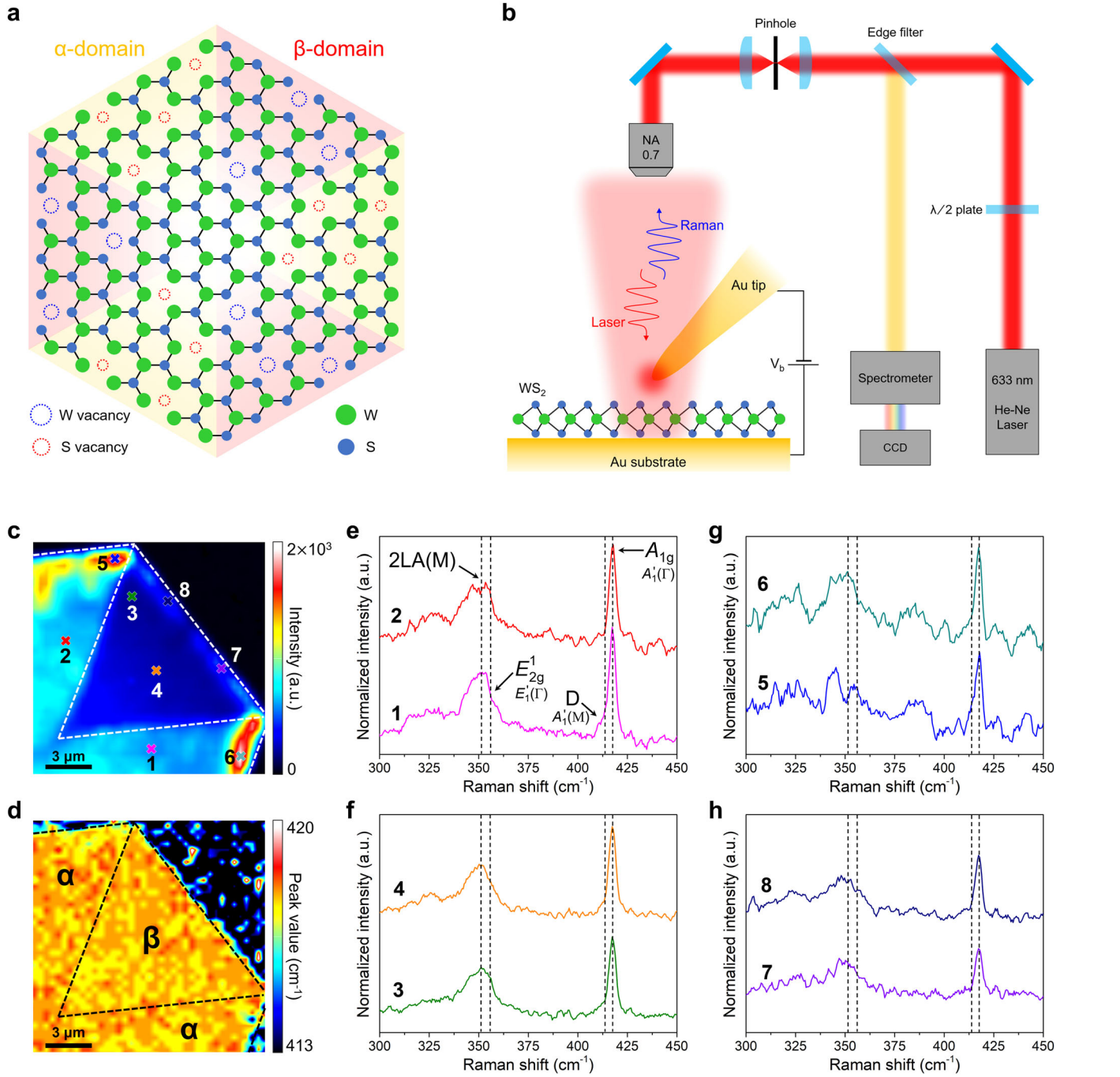

Fig. 1 Raman scattering for monolayer WS_2. **a** Schematic of single-crystalline hexagonal WS_2 monolayer. **b** Schematic of STM-based TERS system with a gap-mode configuration. STM-TERS measurements were performed at a constant-current mode by applying a bias voltage of 50 mV to the sample. **c** Confocal Raman map of A_{1g} peak area intensity with PL background (acquisition time per point: 1 s). **d** Distribution image of A_{1g} peak from the Raman map in (**c**). The white and black dashed lines in **c** and **d** indicate the domain boundaries and edges of WS_2. Confocal Raman spectra from **e** α-domain, **f** β-domain, **g** edge of α-domain, and **h** edge of β-domain. The spectra were extracted from each colored cross in (**c**).

monolayer WS_2 by defects, appears as the shoulder or split peak of the A_{1g} mode and generates spectrum skewness for the A_{1g} mode. Figure 3b shows a large difference in the skewness of A_{1g} peak between the α- and β-domains. The skewness value in the α-domain is positive over the entire region, whereas that in the β-domain is negative. These results for the peak skewness indicate that in the case of positive values, the A_{1g} peak in the α-domain can be fitted using a single Lorentzian function. In the case of negative values, the shoulder or split peaks for the A_{1g} mode appear strongly as the D mode in the β-domain, indicating that the spectrum is highly skewed. Although the negative skewness indicates that the A_{1g} peak is accompanied by the D peak, the weak Raman intensity in the β-domain generates an asymmetric spectrum owing to the low signal-to-noise ratio of the A_{1g} peak. Accordingly, a peak distribution image for the D mode was derived from Fig. 2a to investigate the heterogeneous defects that

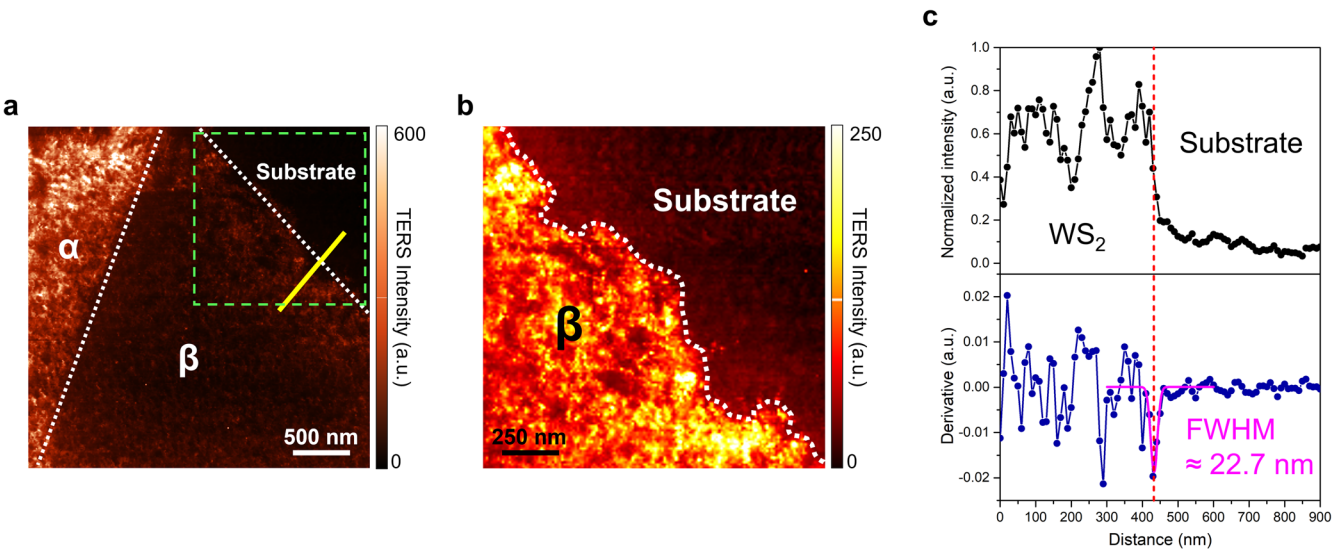

Fig. 2 Spatial resolution of TERS imaging. a TERS map of A_{1g} peak area intensity for monolayer WS_2 with background (acquisition time for point: 0.5 s). The measured region is the same as the confocal Raman map. **b** Magnification of the green dashed square in the TERS image in (**a**). The white dotted curve indicates the sample edge. **c** Normalized TERS intensity profile along a yellow solid bar and the derivative of the intensity profile.

caused the D peak, as shown in Fig. 3c. The D peak distribution image reveals that red-shifted peaks appear in the entire β-domain. This distribution of the red-shifted D peaks and negative skewness in the β-domain can be attributed to a number of $V_{W\text{-}d}$ with V_S.

Furthermore, to thoroughly identify the Raman features of the heterogeneous defects depending on the single-crystalline WS_2 domains, we obtained the TERS spectra from each region marked by the colored (numbered) circles, as shown in Fig. 3d–g. Spectra 1 and 2 in the middle of the α-domain show relatively strong TERS signals along with the intensity of the weak D peak. In Fig. 3d, the A_{1g} mode of spectrum 1, which has a red-shifted shoulder peak in the D mode at 410.2 cm^{-1}, shows a marginally red-shifted peak at ~416.7 cm^{-1}. The A_{1g} peak value of spectrum 2, which barely reveals the shoulder peak, is ~417.1 cm^{-1}, which is equal to the Raman frequency value of the pristine monolayer WS_2. These shifts in the A_{1g} and D peaks were revealed due to a high V_S density[20]. We also analyzed the TERS spectra 3 and 4 in the edge region of the α-domain. The TERS signals of the α-edge region were lower in intensity than those in the middle area of the α-domain. Spectrum 3 in Fig. 3e presents the non-shifted A_{1g} corresponding to the peak value of spectrum 2, whereas spectrum 4 shows the non-shifted A_{1g} peak in conjunction with the red-shifted D peak at ~410.3 cm^{-1}. A comparison between the TERS image and the confocal Raman map reveals a defective edge area in the TERS map (absent in the confocal Raman image) owing to the high spatial resolution of TERS. In these defective edge regions, the energy-shifted D mode without the A_{1g} peak shift can be generated by structural disorders but not V defects causing the A_{1g} mode shift due to the doping effect[47]. Moreover, the TERS spectra 5–8 were extracted from the middle and edge regions of the β-domain. We observe that the β-domain region has more blue-shifted peaks than the α-domain, as shown in Fig. 3a. In addition, a number of red-shifted points related to the D mode (<50 nm in size) are observed in the middle of the β-domain in Fig. 3c. Two spectra were derived from the points, as shown in Fig. 3f. The TERS spectra 5 and 6 for the middle region in the β-domain show red-shifted D peaks with strong intensity as the shoulder peak of the A_{1g} mode. In contrast to the α-domain, the D peaks were accompanied by blue-shifted A_{1g} peaks. The high intensity of the D peak and blue-shifted A_{1g} mode can be explained by $V_{W\text{-}d}$, which produces defect-induced localized states near the valence band[46,48]. Furthermore, the TERS signals at the edge region in the β-domain exhibit a red-shifted D peak and a blue-shifted A_{1g} peak with a broad FWHM. Accordingly, we assume that the blue shift of the Raman frequency and the broader peak width are results of the structural defects of the edge region and $V_{W\text{-}d}$ defects in the β-domain. In addition, magnified TERS mapping reveals a defective edge site in the β-domain, as shown in Fig. 4.

TERS for edge defects

We measured the high-resolution TERS image of a single-crystalline WS_2 monolayer to investigate the properties of the edge defects and the correlation between the D and A_{1g} modes according to the region, as shown in Fig. 4. Although the TERS image in Fig. 4a shows inhomogeneous TERS intensities, we cannot distinguish the difference of Raman peak shifts in the distribution image of Fig. 4b. Accordingly, we extracted the TERS spectra from the basal plane to the Au substrate, including the edge region of the single-crystalline WS_2, as shown in Fig. 4c. The edge region could be divided into specific regions of tens of nanometers. These indicate the inner, edge, and Au regions. These parts were divided by the sample location, and the defective region between the inner parts was designated by the feeble signals in the TERS image in Fig. 4a. The TERS spectra of the inner position displayed intensities stronger than those of the defective and edge regions. In addition, unlike the frequency of 417 cm^{-1} for the D and A_{1g} modes of a defect-free WS_2 monolayer (black dotted line) with each spectrum, the spectra display many blue-shifted peaks, specifically at the defective and edge parts in Fig. 4c. These TERS spectra were deconvoluted into the D and A_{1g} modes using the Lorentzian function to examine the Raman shift and intensity (Supplementary Fig. 10). In accordance with the fitted spectra, we plotted the peak value and intensity for each Raman mode along the tip displacement in Fig. 4d and e. Furthermore, we compared the peak shifts and intensities to reveal the correlation between these values. As shown in Fig. 4d and e, the D and A_{1g} modes with an intrinsic value of 417 cm^{-1} exist as red- and blue-shifted peaks, respectively, from the inner part to the edge of the sample. The peak value and intensity of the D mode exhibit large variations without consistency until the tip position reaches the edge region. Despite the inner region, considering the overall sample, all the inner and edge regions can

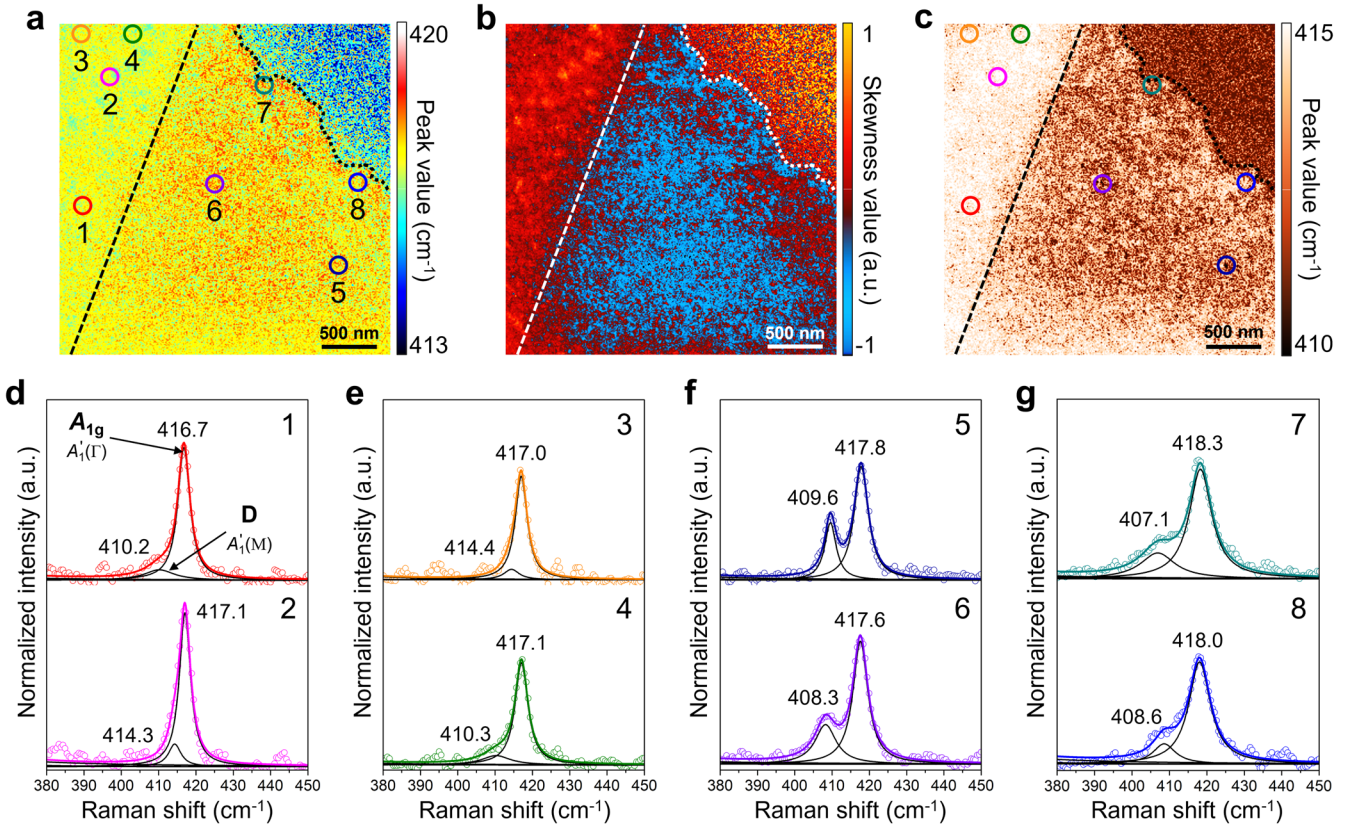

Fig. 3 TERS imaging of monolayer WS_2. **a** Peak distribution image for A_{1g} mode derived from Fig. 2. **b** A_{1g} peak skewness image. **c** Peak distribution image of D mode. TERS spectra were extracted from the **d** middle and **e** edge regions of the α-domain, and the **f** middle and **g** edge regions of the β-domain. Each colored (numbered) circle in the TERS images corresponds to the spectra of the same color (number). These spectra **d**–**g** were fitted using Lorentzian functions.

be regarded as sample edge regions of the β-domain. Accordingly, the structural disorders, as well as the $V_{W\text{-}d}$ defects, are presented, and the variation in peak shift and intensity for the D mode could be generated owing to the density and type of defects. However, the A_{1g} peak shows a blue shift with a gradual increase in the wavenumber when the tip approaches the edge region, as shown in Fig. 4e. This blue shift of the A_{1g} mode with the variation of the D mode indicates that the density of $V_{W\text{-}d}$ defects increases along the spectral line trace from the inner part to the edge region, whereas structural disorders are generally distributed arbitrarily. Furthermore, in the first edge region, the A_{1g} signal with the weakest intensity appears, and the signals include a blue-shifted peak at more than 420 cm^{-1}. The intensity of the D mode presents the strongest signal and a relatively small variation in the peak value. In Fig. 4, although the red-shifted D mode, as a zone-edge phonon mode, is split from the red- or blue-shifted A_{1g} peak and engendered, the strongest intensity and non-shifted peak of the D mode originate in conjunction with the blue-shifted A_{1g} peak at the beginning of the edge region. This edge region represents a significantly small and localized part of the entire sample edge. It contains a high density of various defects, specifically $V_{W\text{-}d}$ defects and broken edges. The $V_{W\text{-}d}$ defects induce blue-shifted A_{1g} peaks, and the broken-edge defects cause strong D peak signals without variation in the Raman shift.

In addition to the localized state generation near the valence or conduction bands, the emergence of the D mode can be explained by a phonon confinement effect such as the momentum conservation rule for a phonon-defect scattering process and relaxation of the selection rule for a first-order Raman process through the phonon weighting function[39,49–51]. In the first-order Raman scattering process, the Raman active mode, as a zone-center optical phonon, can be generated in defect-free crystalline materials when the requirement for momentum conservation is $\mathbf{q} \cong 0$, where $\mathbf{q}$ is a wave vector indicating the phonon momentum. Therefore, defects such as V defects and structural disorders can break the pristine crystalline structure and produce defect-induced nanostructures with a finite phonon correlation length (L_C), causing relaxation of the fundamental Raman selection rule. In other words, the defects introduce the relaxation of the Raman selection rule of $\mathbf{q} \cong 0$, producing a phonon away from the Γ point in the Brillouin zone. In addition, this relaxation could be evaluated using the phonon weighting function $W(r, L_C)$ for the Raman process, where r is the spatial coordinate. This function is expressed as a decay factor of the Gaussian formation as follows[39,49–52]:

$$W(r, L_C) = \exp\left(-ar^2/L_C^2\right), \tag{1}$$

where a is an alterable confinement coefficient representing an attenuation of the phonon amplitude. L_C can be regarded as the size of the defect-induced nanodomain. Based on the weighting function $W(r, L_C)$, the intensity $I(\omega)$ of the first-order Raman mode in 2D nanocrystalline materials can be determined through the phonon confinement model designed by the Richter–Wang–Ley (RWL model)[52]. Moreover, the proposed model can be used to explain the peak shift, FWHM, and skewness of the peak for the first-order Raman process as follows[39,49–52]:

$$I(\omega) \propto \int \frac{|C(\mathbf{q})|^2}{(\omega - \omega(\mathbf{q}))^2 + (\Gamma_0/2)^2} \mathrm{d}\mathbf{q}, \tag{2}$$

where $C(\mathbf{q})$ is the Fourier coefficient of the weighting function $W(r, L_C)$, and $\omega(\mathbf{q})$ is the phonon dispersion curve in the infinite domain induced by defects, Γ_0 is the natural width of the Raman peaks,

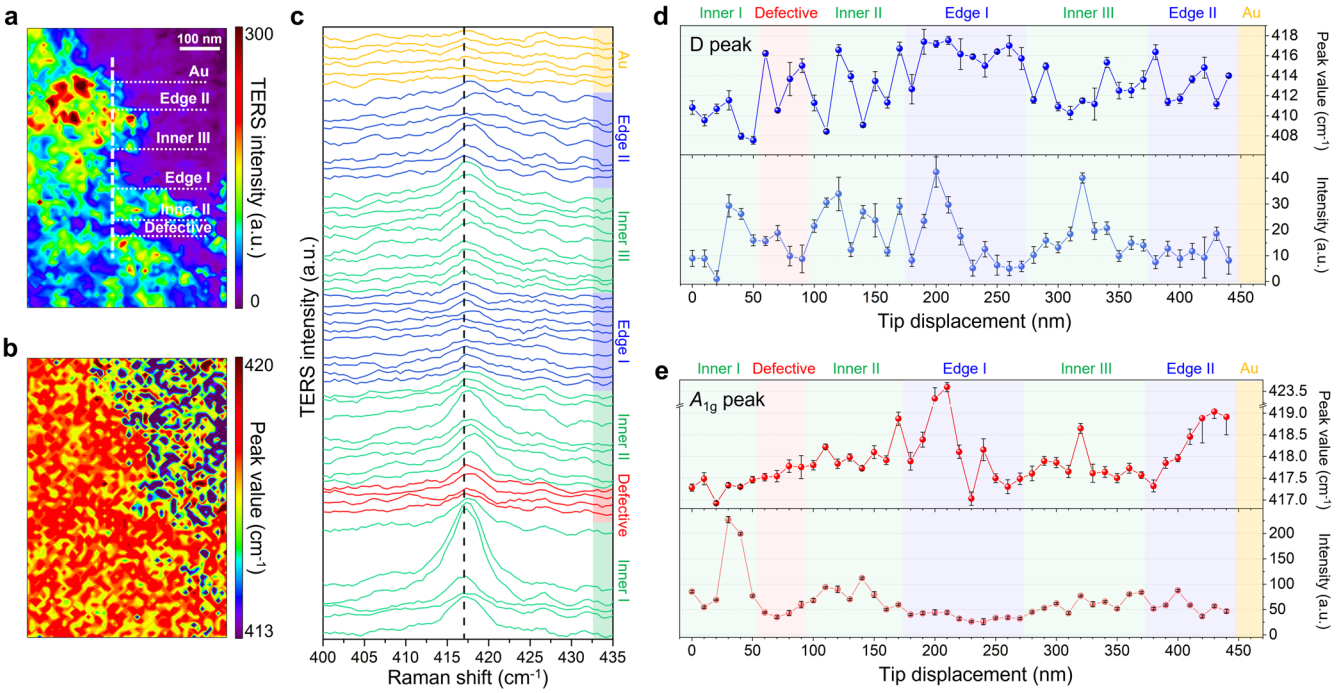

Fig. 4 TERS imaging for the localized edge region. a High-resolution TERS image for A_{1g} peak area intensity. The white dashed line indicates the positions of the extracted TERS spectra in (**c**). **b** Peak distribution TERS image derived from (**a**). **c** TERS spectral line trace for D and A_{1g} peaks. Each TERS spectrum was extracted at an interval of 10 nm. The black dashed line indicates the Raman shift of 417 cm^{-1}. Plots of peak values and intensities for **d** D peak and **e** A_{1g} peak, with respect to tip displacement. The error bars indicate the fitting error.

and the integral indicates integration over the entire range of the Brillouin zone. Thus, Eq. (2) indicates the weighted integration of the Raman peaks of the Lorentzian function based on the phonon dispersion $\omega(\mathbf{q})$. Equation (2) can be approximated as follows for a 2D nanostructure using the attenuation factor for a Gaussian function in Eq. (1)[39,49–52]:

$$I(\omega) = \int \frac{\exp\left(-q^2 L_C^2/2a\right)}{\left(\omega - \omega(\mathbf{q})\right)^2 + \left(\Gamma_0/2\right)^2} 2\pi q \, \mathrm{d}\mathbf{q}. \quad (3)$$

According to Eq. (3) for the phonon confinement model, $\mathbf{q} \neq 0$ phonons can be quantified in the Raman process[39]. The A_{1g} mode of the out-of-plane optical (ZO) branch can be degenerated at the Γ point, where the dispersion curve for the degenerated phonon indicates the D mode of the ZO branch at the M point in the Brillouin zone[39,49]. Therefore, V defects and structural defects can alter the lattice structures of a single-crystalline WS_2 monolayer. Moreover, a variation in the lattice structure (such as broken-edge defects) induces a finite L_C so that a zone-edge phonon similar to the D mode can occur while satisfying momentum conservation and the Raman selection rule.

In addition, the inner II and inner III regions exhibit blue-shifted A_{1g} peaks of weak signals without fluctuation, accompanied by the D mode, including the variable peak value and intensity, as shown in Fig. 4e. Moreover, in the edge II region, the blue-shift of the A_{1g} peak occurs with a gradual increase in the wavenumber as the tip moves toward the Au region. This implies that the end part of the edge region contained a higher density of $V_{W\text{-}d}$ defects than its inner part.

Quantum mechanical calculation for heterogeneous defects

We conducted quantum mechanical calculations within the DFT framework to investigate the effect of heterogeneous defects such as $V_{S\text{-}d}$ and $V_{W\text{-}d}$ defects on the Raman vibrational modes in monolayer WS_2[20]. First, we performed DFT calculations for an ideal defect-free WS_2 to identify the vibrational direction and value of the Raman frequency for a general A_{1g} peak (Supplementary Fig. 11). The Raman frequency for the A_{1g} mode was calculated to be 413.41 cm^{-1} (Supplementary Table 1). We established two types of models for the $V_{S\text{-}d}$ and $V_{W\text{-}d}$ defects based on the calculations for the ideal model, to examine the change in vibrational modes and Raman frequencies. Figure 5a shows the monolayer WS_2 structure with a $V_{S\text{-}d}$ defect, which indicates one V_W with six neighboring V_S (V_{W1S6}). In the case of the V_{W1S6} defect, we can observe out-of-plane vibrations for the A_{1g} and D modes[20], as shown in Fig. 5b and c. The A_{1g} mode shows a weakened vibrational range, and the Raman frequency is calculated to be 412.77 cm^{-1} (Supplementary Table 1). Although V_W can introduce the blue-shifted A_{1g} mode owing to the generation of localized states near the valence band, the A_{1g} mode for V_{W1S6} exhibits a lower energy value than pristine monolayer WS_2. This implies that the Raman frequency is red-shifted by the n-doping effect and that the V_{S6} adjoining V_W has a significantly higher doping effect. Moreover, asymmetric vibration of the D mode can also be generated by the V_{W1S6} defect, as shown in Fig. 5c. The value of the D mode was estimated to be 409.27 cm^{-1} via DFT calculations (Supplementary Table 1). In addition, we performed DFT calculations for $V_{W\text{-}d}$ defects such as the two single V_W defects ($2V_W$) and the V_{W1S6} defect (Fig. 5d). These were performed because the β-domain contains $V_{W\text{-}d}$, which induces blue-shifted A_{1g} and red-shifted D peaks. Out-of-plane vibrations can occur in the localized region of the cell, as shown in Fig. 5e (Supplementary Fig. 12). This directional vibration can also be regarded as the A_{1g} mode because the blue vectors are perpendicular to the *a*- and *b*-axes and parallel to the *c*-axis in the crystal structure[53]. The calculated A_{1g} mode has a blue-shifted Raman frequency of 416.64 cm^{-1} (Supplementary Table 1). In addition, the $2V_W$ defects generated both blue-shifted A_{1g} and red-shifted D modes of 407.06 cm^{-1} (Fig. 5f; Supplementary Table 1). These shifted values for the V-induced Raman peaks are close to the experimental results. Thus, we demonstrated that various heterogeneous defects such as structural disorders $V_{S\text{-}d}$, $V_{W\text{-}d}$, and edge defects in single-crystalline WS_2 can produce different Raman vibrational properties in conjunction with the appearance of the D mode.

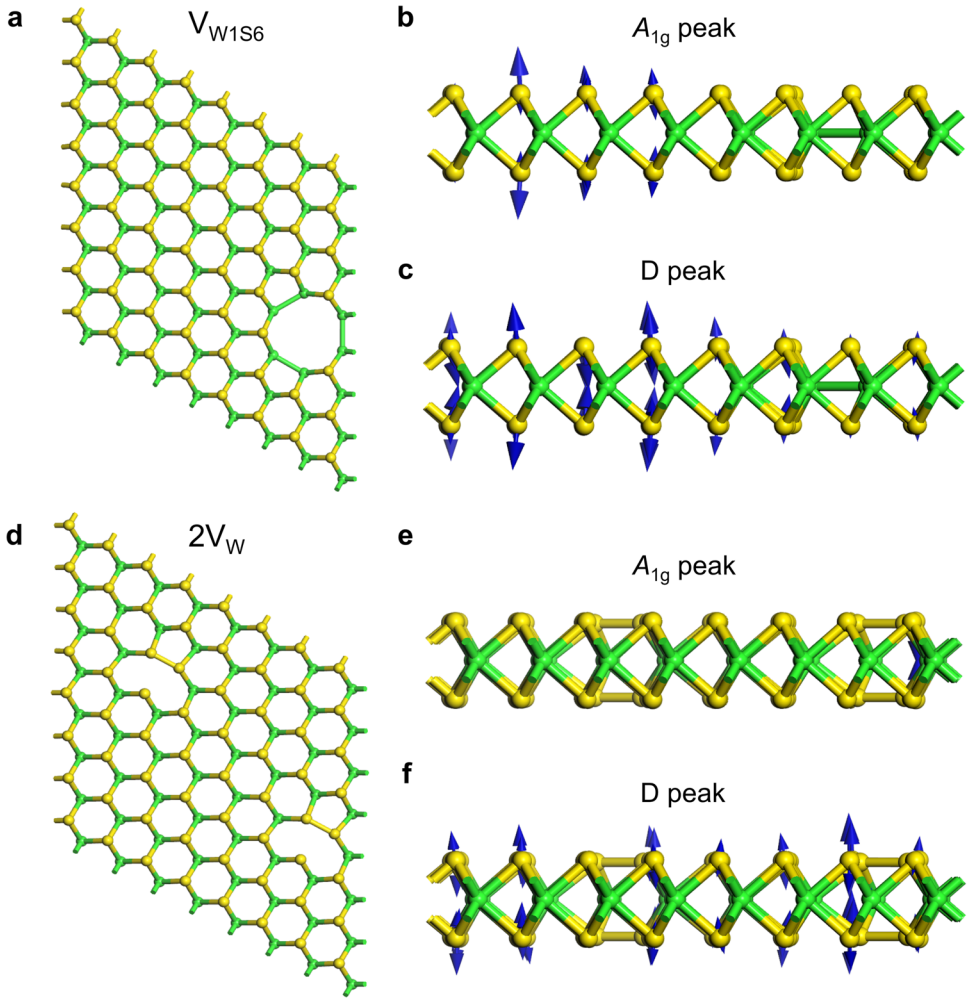

Fig. 5 DFT calculations for the Raman modes induced by $V_{S\text{-}d}$ and $V_{W\text{-}d}$ defects. a Complex vacancies model for 1 V_W with 6 V_S in the 8×8 unit cell. V_{W1S6}-induced vibrational modes for **b** A_{1g} and **c** D peaks. **d** Two single V_W model in the 8×8 cell. $2V_W$-induced vibrational modes for **e** A_{1g} peak and **f** D peak. The blue arrows indicate the vectors for the atomic vibrations. The vector length does not indicate the Raman intensity.

DISCUSSION

In this study, we investigated the heterogeneous defects in a single-crystalline WS_2 monolayer using STM-based TERS imaging. We demonstrated heterogeneous defect-induced Raman signals for α- and β-domains and edges. In the case of the α-domain, $V_{S\text{-}d}$ defects were distributed such that red-shifted A_{1g} and D modes are observed. In the case of the β-domain, the blue-shifted A_{1g} mode is accompanied by a red-shifted D mode because $V_{W\text{-}d}$ defects are the majority defect in the β-domain. Furthermore, the β-domain exhibited a relatively higher D mode intensity than the α-domain. This intensity differential, in the narrow region below several tens of nanometers, indicates that the density of nanoscale defects in the β-domain significantly exceeds the defect density in the α-domain. In addition, it was revealed that the edge defects, which can occur straightforwardly owing to CVD synthesis, were structural disorders using high-spatial-resolution TERS imaging. The D mode was generated by these edges in addition to the V defects. These results imply that TERS exhibits substantial potential as a nondestructive nanoscale imaging technique for investigating the optical properties of nanoscale defects in monolayer WS_2 as well as other 2D layered semiconductors.

METHODS

Synthesis of single-crystalline WS_2 monolayer

Hexagonal monolayer WS_2 samples were synthesized using CVD[18]. Ammonium metatungstate hydrate (Sigma-Aldrich) was used as a precursor, and sodium cholate hydrate (Sigma-Aldrich) was used as a promoter. Each material was dissolved separately in deionized (DI) water. The solutions were then mixed with a medium solution (OptiPrep density gradient medium; Sigma-Aldrich). The mixed solution was dropped onto a SiO_2/Si substrate and spin-coated. The W precursor-coated substrate and S powder (Sigma-Aldrich) were placed at two different positions in a CVD chamber and heated uniformly to 780 and 210 °C, respectively, in a furnace under atmospheric pressure.

Fabrication of Au tip for TERS

The Au tip was fabricated via electrochemical etching[54,55]. An Au wire with a diameter of 250 μm (Nilaco) was used to fabricate the tip. A mixed solution consisting of 37% hydrochloric acid solution (Sigma-Aldrich) and anhydrous ethanol (Sigma-Aldrich) was used as an etchant to etch the Au wire. A wave-function generator with a frequency of 300 Hz and a 20% duty cycle supplied a pulsed voltage from −25 mV to 3.5 V. After etching, four solutions (acetone, ethanol, DI water, and isopropanol) were used separately to rinse the etched Au tip.

Confocal Raman scattering and TERS measurements

Confocal Raman scattering of monolayer WS_2 was measured using a confocal Raman microscope system (XperRAM C, Nanobase & NTEGRA Spectra, NT-MDT). This equipment (NTEGRA Spectra, NT-MDT) was also used to conduct the TERS experiment by combining the confocal Raman and STM systems. In all the experiments, an objective lens with an NA of 0.7 and magnification of ×100 (Mitutoyo) was used to irradiate the WS_2 monolayer with an excitation laser of wavelength 633 nm (<0.7 mW). The laser, which was linearly polarized in the confocal measurement, was polarized along the Au tip axis as well in the TERS experiment. The Raman scattering signals were acquired using a charge-coupled device detector (Andor) cooled to −80 °C and a spectrometer with 1800 grooves/mm grating. The thermal drift of the piezoelectric scanner was approximately 15 nm/min/°C for the *XY*-axis and 10 nm/min/°C for the *Z*-axis. The scanner was warmed for 1 day prior to the TERS experiment (step size of 10 nm) to avoid thermal drift. The measurements were conducted under ambient conditions.

DFT calculations for vibration modes of defective monolayer WS_2

Quantum mechanical calculations were performed via DFT using the basis sets for atomic orbitals following the DMOL3 code on the BIOVIA Materials Studio platform[20,56]. We used the double with polarization form for the basis sets of atomic orbitals. During the calculation, we considered all the electrons containing the core parts. Exchange-correlation functions were obtained using the local density approximation and *k*-points with a Monkhorst–Pack grid with a separation of 0.02/Å. The criteria of distance, force, and total energy difference for geometry optimization were 0.005 Å, 0.001 Ha/Å, and 10^{-5} Ha, respectively. The bulk WS_2 geometry was obtained using ICSD as the lattice parameter: $a = 3.154$ Å, $b = 3.154$ Å, $c = 12.360$ Å, $\alpha = 90°$, $\beta = 90°$, and $\gamma = 120°$. Using this initial geometry, we minimized it fully, including the cell optimization. We obtained the following lattice parameters: $a = 3.1959$ Å, $b = 3.1959$ Å, $c = 11.3908$ Å, $\alpha = 90°$, $\beta = 90°$, and $\gamma = 120°$. An 8×8 unit cell was produced from the optimal geometry, and one monolayer was eliminated to obtain the monolayer WS_2 geometry. We fully relaxed this geometry again to achieve the reference system of the energetically stable state for further calculations. Using the ideal reference system, the initial geometries were generated with $2V_W$ by removing two W atoms and V_{W1S6} and full relaxation of the geometry. The optimized bond lengths at the V_{W1S6} defect were 2.67 Å for the W–W bond and 2.43 Å for the W–S bond. The hole size of V_{W1S6} was 6.34 Å.

We analyzed the vibrations based on these conditions using the optimized geometries of the ideal WS_2, $2V_W$, and V_{W1S6}. We computed the vibrational frequencies of monolayer WS_2 using mass-weighted second-derivative Cartesian matrix diagonalization (i.e., Hessian matrix)[57]. We computed Hessian elements by replacing each atom and then, calculating a gradient vector. A complete second-derivative matrix was thus built according to the computational scheme. Thus, the vibrational modes were numerically calculated. Using a two-point difference, Hessian was estimated to reduce numerical rounding errors. We extracted the intensities from the atomic polar tensor, which indicates the second derivative of the total energy in terms of dipole moments and Cartesian coordinates. The intensities for each mode were estimated as the square of the transition moments for each mode. In addition, these were expressed with respect to the atomic polar tensor matrix and mass-weighted Hessian eigenvectors. The displacement step size was set at 0.005 Å.

DATA AVAILABILITY

The data that support the findings of this study are available from the corresponding author upon reasonable request.

Received: 30 January 2022; Accepted: 1 August 2022;
Published online: 16 September 2022

REFERENCES

1. Wang, Q. H., Kalantar-Zadeh, K., Kis, A., Coleman, J. N. & Strano, M. S. Electronics and optoelectronics of two-dimensional transition metal dichalcogenides. *Nat. Nanotechnol.* **7**, 699–712 (2012).
2. Mak, K. F. et al. Tightly bound trions in monolayer MoS_2. *Nat. Mater.* **12**, 207–211 (2013).
3. Hong, X. et al. Ultrafast charge transfer in atomically thin MoS_2/WS_2 heterostructures. *Nat. Nanotechnol.* **9**, 682–686 (2014).
4. Keum, D. H. et al. Bandgap opening in few-layered monoclinic $MoTe_2$. *Nat. Phys.* **11**, 482–486 (2015).
5. Sie, E. J. et al. Large, valley-exclusive Bloch–Siegert shift in monolayer WS_2. *Science* **355**, 1066–1069 (2017).
6. Gong, S.-H., Alpeggiani, F., Sciacca, B., Garnett, E. C. & Kuipers, L. Nanoscale chiral valley-photon interface through optical spin–orbit coupling. *Science* **359**, 443–447 (2018).
7. Jones, A. M. et al. Optical generation of excitonic valley coherence in monolayer WSe_2. *Nat. Nanotechnol.* **8**, 634–638 (2013).
8. Fiori, G. et al. Electronics based on two-dimensional materials. *Nat. Nanotechnol.* **9**, 768–779 (2014).
9. Duong, N. T. et al. Modulating the functions of $MoS_2/MoTe_2$ van der Waals heterostructure *via* thickness variation. *ACS Nano* **13**, 4478–4485 (2019).
10. Mak, K. F., McGill, K. L., Park, J. & McEuen, P. L. The valley Hall effect in MoS_2 transistors. *Science* **344**, 1489–1492 (2014).
11. Zhang, Y., Oka, T., Suzuki, R., Ye, J. & Iwasa, Y. Electrically switchable chiral light-emitting transistor. *Science* **344**, 725–728 (2014).
12. Xu, X., Yao, W., Xiao, D. & Heinz, T. F. Spin and pseudospins in layered transition metal dichalcogenides. *Nat. Phys.* **10**, 343–350 (2014).
13. Mak, K. F. & Shan, J. Photonics and optoelectronics of 2D semiconductor transition metal dichalcogenides. *Nat. Photonics* **10**, 216–226 (2016).
14. Bang, S. et al. Augmented quantum yield of a 2D monolayer photodetector by surface plasmon coupling. *Nano Lett.* **18**, 2316–2323 (2018).
15. An, S.-J., Kim, Y. H., Lee, C., Park, D. Y. & Jeong, M. S. Exfoliation of transition metal dichalcogenides by a high-power femtosecond laser. *Sci. Rep.* **8**, 1–6 (2018).
16. Kang, K. et al. High-mobility three-atom-thick semiconducting films with wafer-scale homogeneity. *Nature* **520**, 656–660 (2015).
17. Lee, J. S. et al. Wafer-scale single-crystal hexagonal boron nitride film *via* self-collimated grain formation. *Science* **362**, 817–821 (2018).
18. Jeong, H. Y. et al. Heterogeneous defect domains in single-crystalline hexagonal WS_2. *Adv. Mater.* **29**, 1605043 (2017).
19. Lin, Y. C. et al. Revealing the atomic defects of WS_2 governing its distinct optical emissions. *Adv. Funct. Mater.* **28**, 1704210 (2018).
20. Lee, C. et al. Unveiling defect-related Raman mode of monolayer WS_2 *via* tip-enhanced resonance Raman scattering. *ACS Nano* **12**, 9982–9990 (2018).
21. Parkin, W. M. et al. Raman shifts in electron-irradiated monolayer MoS_2. *ACS Nano* **10**, 4134–4142 (2016).
22. Hong, J. et al. Exploring atomic defects in molybdenum disulphide monolayers. *Nat. Commun.* **6**, 1–8 (2015).
23. Roy, S. et al. Atomic observation of filling vacancies in monolayer transition metal sulfides by chemically sourced sulfur atoms. *Nano Lett.* **18**, 4523–4530 (2018).
24. Bao, W. et al. Visualizing nanoscale excitonic relaxation properties of disordered edges and grain boundaries in monolayer molybdenum disulfide. *Nat. Commun.* **6**, 1–7 (2015).
25. Ly, T. H. et al. Misorientation-angle-dependent electrical transport across molybdenum disulfide grain boundaries. *Nat. Commun.* **7**, 1–7 (2016).
26. Van Der Zande, A. M. et al. Grains and grain boundaries in highly crystalline monolayer molybdenum disulphide. *Nat. Mater.* **12**, 554–561 (2013).
27. Ly, T. H., Zhao, J., Cichocka, M. O., Li, L.-J. & Lee, Y. H. Dynamical observations on the crack tip zone and stress corrosion of two-dimensional MoS_2. *Nat. Commun.* **8**, 1–7 (2017).
28. Betzig, E., Trautman, J. K., Harris, T., Weiner, J. & Kostelak, R. Breaking the diffraction barrier: optical microscopy on a nanometric scale. *Science* **251**, 1468–1470 (1991).
29. Zhong, J.-H. et al. Probing the electronic and catalytic properties of a bimetallic surface with 3 nm resolution. *Nat. Nanotechnol.* **12**, 132–136 (2017).
30. Park, K. D., Raschke, M. B., Atkin, J. M., Lee, Y. H. & Jeong, M. S. Probing bilayer grain boundaries in large-area graphene with tip-enhanced Raman spectroscopy. *Adv. Mater.* **29**, 1603601 (2017).
31. Rahaman, M. et al. Highly localized strain in a MoS_2/Au heterostructure revealed by tip-enhanced Raman spectroscopy. *Nano Lett.* **17**, 6027–6033 (2017).
32. Bhattarai, A. et al. Tip-enhanced Raman scattering from nanopatterned graphene and graphene oxide. *Nano Lett.* **18**, 4029–4033 (2018).
33. Liao, M. et al. Tip-enhanced Raman spectroscopic imaging of individual carbon nanotubes with subnanometer resolution. *Nano Lett.* **16**, 4040–4046 (2016).
34. Park, K.-D., Jiang, T., Clark, G., Xu, X. & Raschke, M. B. Radiative control of dark excitons at room temperature by nano-optical antenna-tip Purcell effect. *Nat. Nanotechnol.* **13**, 59–64 (2018).
35. Park, K.-D. et al. Hybrid tip-enhanced nanospectroscopy and nanoimaging of monolayer WSe_2 with local strain control. *Nano Lett.* **16**, 2621–2627 (2016).
36. Park, K.-D. et al. Tip-enhanced strong coupling spectroscopy, imaging, and control of a single quantum emitter. *Sci. Adv.* **5**, eaav5931 (2019).

37. Lee, J., Crampton, K. T., Tallarida, N. & Apkarian, V. A. Visualizing vibrational normal modes of a single molecule with atomically confined light. *Nature* **568**, 78–82 (2019).
38. Zhang, R. et al. Chemical mapping of a single molecule by plasmon-enhanced Raman scattering. *Nature* **498**, 82–86 (2013).
39. Shi, W. et al. Raman and photoluminescence spectra of two-dimensional nanocrystallites of monolayer WS_2 and WSe_2. *2D Mater.* **3**, 025016 (2016).
40. Li, J. et al. Atypical defect-mediated photoluminescence and resonance Raman spectroscopy of monolayer WS_2. *J. Phys. Chem. C* **123**, 3900–3907 (2019).
41. Kim, M. S. et al. Biexciton emission from edges and grain boundaries of triangular WS_2 monolayers. *ACS Nano* **10**, 2399–2405 (2016).
42. Chow, P. K. et al. Defect-induced photoluminescence in monolayer semiconducting transition metal dichalcogenides. *ACS Nano* **9**, 1520–1527 (2015).
43. Nan, H. et al. Strong photoluminescence enhancement of MoS_2 through defect engineering and oxygen bonding. *ACS Nano* **8**, 5738–5745 (2014).
44. Gutiérrez, H. R. et al. Extraordinary room-temperature photoluminescence in triangular WS_2 monolayers. *Nano Lett.* **13**, 3447–3454 (2013).
45. Huang, T.-X. et al. Probing the edge-related properties of atomically thin MoS_2 at nanoscale. *Nat. Commun.* **10**, 1–8 (2019).
46. Salehi, S. & Saffarzadeh, A. Atomic defect states in monolayers of MoS_2 and WS_2. *Surf. Sci.* **651**, 215–221 (2016).
47. Staiger, M. et al. Excitonic resonances in WS_2 nanotubes. *Phys. Rev. B* **86**, 165423 (2012).
48. Qiu, H. et al. Hopping transport through defect-induced localized states in molybdenum disulphide. *Nat. Commun.* **4**, 1–6 (2013).
49. Mignuzzi, S. et al. Effect of disorder on Raman scattering of single-layer MoS_2. *Phys. Rev. B* **91**, 195411 (2015).
50. Zi, J., Zhang, K. & Xie, X. Comparison of models for Raman spectra of Si nanocrystals. *Phys. Rev. B* **55**, 9263 (1997).
51. Campbell, I. & Fauchet, P. M. The effects of microcrystal size and shape on the one phonon Raman spectra of crystalline semiconductors. *Solid State Commun.* **58**, 739–741 (1986).
52. Richter, H., Wang, Z. & Ley, L. The one phonon Raman spectrum in microcrystalline silicon. *Solid State Commun.* **39**, 625–629 (1981).
53. Staiger, M. et al. Splitting of monolayer out-of-plane A 1′ Raman mode in few-layer WS_2. *Phys. Rev. B* **91**, 195419 (2015).
54. Lee, C. et al. Tip-enhanced Raman scattering imaging of two-dimensional tungsten disulfide with optimized tip fabrication process. *Sci. Rep.* **7**, 1–7 (2017).
55. Kim, D. H., Lee, C., Jeong, B. G., Kim, S. H. & Jeong, M. S. Fabrication of highly uniform nanoprobe *via* the automated process for tip-enhanced Raman spectroscopy. *Nanophotonics* **9**, 2989–2996 (2020).
56. Delley, B. From molecules to solids with the DMol 3 approach. *J. Chem. Phys.* **113**, 7756–7764 (2000).
57. Wilson, E., Decius, J. & Cross, P. *Molecular Vibrations*. (Dover Publications, Inc, New York, 1980).

ACKNOWLEDGEMENTS

This research was supported by Basic Science Research Program through the National Research Foundation of Korea (NRF) funded by Korean government (MSIP) (2022M3F3A2A01072215), the commercialization Promotion Agency for R&D Outcomes (COMPA) funded by the Ministry of Science and ICT (MSIT) (2022-URE-07), and a National Research Council of Science & Technology (NST) grant by the Korean Government (MSIT) (No. CAP-18-04-KRISS).

AUTHOR CONTRIBUTIONS

C.L. and M.S.J. conceived and designed the study. C.L., B.G.J., and S.H.K. performed most of the experiments, including the TERS, tip fabrication, characterization, and data analysis. D.H.K. performed the tip fabrication. S.-J.A. and D.L. conducted the AFM analysis. W.C. and Y.-M.K. performed the TEM analysis. S.J.Y. and K.K.K. performed the CVD growth of 1L-WS_2. S.M.L. performed the DFT calculations. C.L. wrote the manuscript. S.M.L. led the theory group; and M.S.J. organized the project and led the experimental group. All the authors have discussed the results and commented on the manuscript.

COMPETING INTERESTS

The authors declare no competing interests.

ADDITIONAL INFORMATION

Supplementary information The online version contains supplementary material available at https://doi.org/10.1038/s41699-022-00334-4.

Correspondence and requests for materials should be addressed to Seung Mi Lee or Mun Seok Jeong.

Reprints and permission information is available at http://www.nature.com/reprints

Publisher's note Springer Nature remains neutral with regard to jurisdictional claims in published maps and institutional affiliations.